Bachelor's Thesis, 15hp

Determination of Proton Beam Waist Positions Using Beam Position Monitors

Presented by:
Gustav Gird Fahlström

Supervisors:
Natalia Milas
Francesca Curbis

Department of Physics

November 2, 2021

Abstract

In this work, we examine a novel method for the determination of proton beam waist locations using beam position monitors. Based on the lattice of the final transport line section of the European Spallation Source linac, a simplified version of the beam line composed of quadrupole magnets and correctors is constructed in Python using a matrix formalism. With a known set of Courant-Snyder parameters at the final position of the beam line and a known beam emittance, a set of final beam centroid positions are calculated lying over the 1σ phase space ellipse at that point. Applying the initial condition that all beam centroids are initially placed at the origin, the necessary corrector strength values required to transport the centroids to their final positions along the ellipse are then calculated by solving a coupled system of equations. Beam centroid trajectories are then plotted along with the beam envelope. Space charge effects are shown to be negligible for this work, meaning that beam centroid waist positions will coincide with envelope waist positions. Two BPMs position readings are then used to calculate the waist location. The method presented in this work reliably determines waist locations with the most significant deviations from benchmark values being 0.03 m for the design lattice and 0.14 m for a lattice featuring significant quadrupole errors.

Acknowledgements

I would like to thank my supervisor, Natalia Milas, for not only being an absolutely stellar supervisor, but also for her practically infinite patience no matter how basic the question, and for her guidance. I would also like to thank Francesca Curbis, also my supervisor, for her valuable feedback and expertise. Thank you both for the hours you put in, and for introducing me to the field.

I would like to thank the entire Beam Physics Section at the ESS for being incredibly welcoming, warm, and helpful. Special thanks to Mamad Eshraqi and Ryoichi Myiamoto for taking the time to advise and provide valuable feedback.

Finally, I would like to thank my fiancée, Jamie DeMarco, for her support, love, and for bearing with me these past few months as I spent the vast majority of my waking hours in front of my laptop.

Contents

Acronyms

A2T Accelerator to Target. 5–10, 15–20, 24

BPM Beam Position Monitor. 1, 5, 6, 8, 9, 16, 20, 24

DTL Drift Tube Linac. 5

ESS European Spallation Source. 5, 8, 10, 15

HEBT High-Energy Beam Transport. 5

LEBT Low Energy Beam Transport. 5

MEBT Medium Energy Beam Transport. 5

RFQ Radio Frequency Quadrupole. 5

1. Introduction

The European Spallation Source (ESS) is a research facility located in Lund, Sweden, consisting of a 600 m long linear accelerator, or linac, a rotating tungsten core, and a series of experimental stations. Protons are accelerated to speeds of almost 95% the speed of light before colliding with the tungsten target, generating large amounts of high-energy neutrons via a process known as spallation. The neutrons are then guided into various other sections of the facility, each containing its own set of optics and diagnostics. There, scientists will be able to use the neutrons to study issues ranging from environmental science and archaeology to the physics of complex materials.

The linac itself consists of several sections, illustrated below in Fig. 1. Protons are generated at an ion source with an energy of 75 keV and are transported along the Low Energy Beam Transport (LEBT) to the first acceleration station, the Radio Frequency Quadrupole (RFQ). In the RFQ the proton beam is accelerated to 3.6 MeV and bunched. The beam then continues along the Medium Energy Beam Transport (MEBT) which contains enough diagnostics to match it to the next accelerating structure, the Drift Tube Linac (DTL). The DTL is a 39 m long accelerating structure that bring the proton beam energy up to 90 MeV. The end of the DTL also marks the end of the normal conducting linac, and from this point on-wards, accelerating structures are of the superconducting (SC) type, operating at 2 K. The first superconducting structures are the Spokes which accelerate the beam to 216 MeV, followed by the Medium-β section, further accelerating the protons to 570 MeV. The final accelerating structure, the High-β section, brings the beam to its nominal energy of 2 GeV. At the end of the linac, the High-Energy Beam Transport (HEBT) guides the proton beam to the dogleg, and also acts as a contingency space for possible upgrades. The dogleg is a vertical chicane, which brings the proton beam up to the target level. The Accelerator to Target (A2T) is the final transport line, focusing and preparing the beam to pass through an aperture within a separating wall before it collides with the tungsten target.

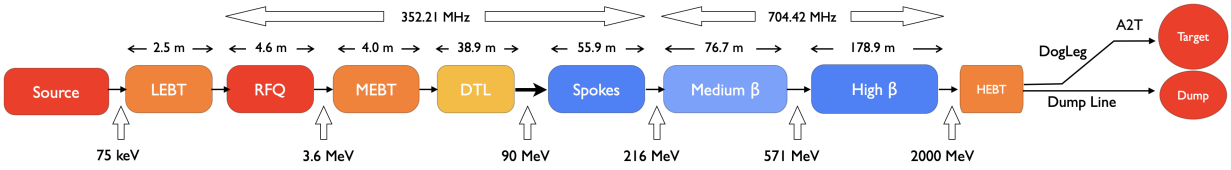

Figure 1: Schematic of the ESS Linac [3]

This work treats the last and final section, the A2T, which is a transfer line. No acceleration occurs in the A2T, and therefore protons enter this section at their nominal energy of 2 GeV. The main diagnostics available at the end of the A2T are two Beam Position Monitor (BPM)s, the first of which is 3 m before the separating wall and the second which is located exactly at the wall position. Further details are given in Section 2.2 Fig. 4. The separating wall imposes an aperture restriction, where the beam must form a waist at that position. An example of waist formation is shown in Fig. 2. The longitudinal position of the waist depends directly on the quadrupole magnet settings in the A2T, and as such, if there are any errors in the beam line, the waist position will shift. The goal of this work is to investigate the viability of determining the beam waist longitudinal position using

only the two final BPMs.

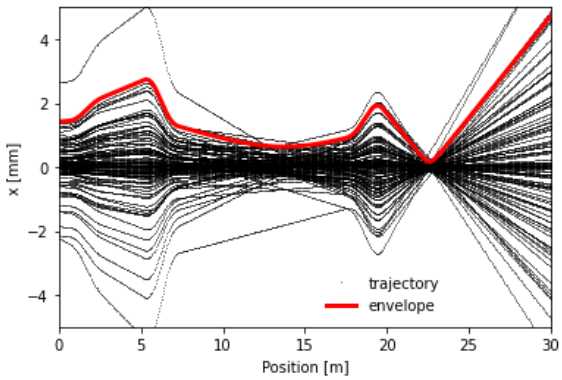

Figure 2: Longitudinal trajectories (in black) and beam envelope (in red) along the A2T lattice.

The following chapter of this work will explore the chosen coordinate system, the A2T and then proceed with the necessary transverse beam dynamics and equations of motion required for modelling the A2T. It then proceeds with the matrix formalism of the A2T elements and the beam line. The third chapter contains the methods and programs used in order to perform the simulations. The fourth chapter includes the main results of this work. The fifth, and final, chapter is dedicated to a discussion of the results and their implications, as well as the future outlook.

2. Transverse Beam Dynamics on a Transfer Line

This section will first examine the A2T and present a short derivation of the transverse beam dynamics equations relevant for this work. The derivation for the matrix representation of the quadrupole and correcter magnets will be presented, along with the matrix representation and construction of the complete beam line.

2.1. Coordinate System

Our choice of coordinate system defines displacements and angles on the transverse positions with respect to a design trajectory. Let the longitudinal displacement along the design trajectory be denoted by s. The transverse phase space coordinates $(u, u'), u \in \{x, y\}$ are used, where u' is defined as:

$$\begin{aligned} u' &\equiv \frac{du}{dt}\frac{dt}{ds} = \frac{du}{ds} = \frac{v_u}{v_s} = \frac{p_u}{p_s} \approx \frac{p_u}{p}, \\ u'' &\equiv \frac{d^2u}{ds^2} \quad . \end{aligned} \tag{1}$$

The coordinate u' is the ratio of transverse to longitudinal momenta, and can be interpreted as the angle between the particle velocity vector and the s coordinate unit vector. u'' is then simply its derivative with respect to s. The substitution of the independent variable $t \to s$ is warranted as the amplitude u and angle u' of a particle trajectory are critical, and therefore the derivatives of u with respect to the reference trajectory s are desired. The subsequent simplifications are justified by the application of the paraxial approximation [8], wherein the transverse momenta p_x and p_y are assumed to be relatively small in comparison to p_z, and so the total momentum p can be approximated by:

$$p = \sqrt{p_x^2 + p_y^2 + p_s^2} \approx \sqrt{p_s^2} \approx p_s \quad . \tag{2}$$

This approximation is well suited for high-energy beams as beam divergence is relatively small [6].

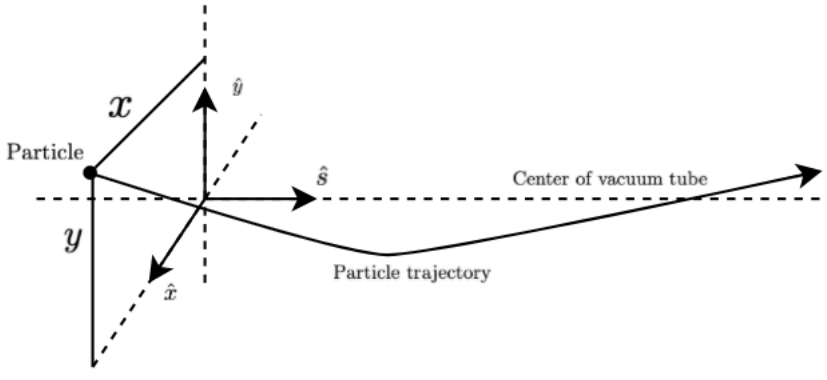

Figure 3: Coordinate system diagram including a test particle trajectory.

In summary, a coordinate system of (u, u', s) is chosen, where u, u' are the displacement and angular divergence, respectively, from a design trajectory, with the coordinate s representing the longitudinal displacement along the beam line. An illustration of the chosen coordinate system is shown in Fig. 3.

2.2. A closer Look at the ESS A2T Lattice

The A2T is the final section of the ESS linac, before the proton beam collides with the target. The purpose of this section of the linac is to successfully guide the proton beam through an aperture in the wall separating the accelerator from the target. It achieves this by using a set of 6 quadrupole magnets for beam focusing, and 4 corrector magnets to ensure a proper beam centroid trajectory. Also included is a set of 6 BPMs and 8 raster magnets. The raster system is used to increase the beam footprint on the target and reduce the peak energy deposition on the target outer shell. For the purposes of this thesis, only the quadrupole magnets, correctors and the final two BPMs will be considered.

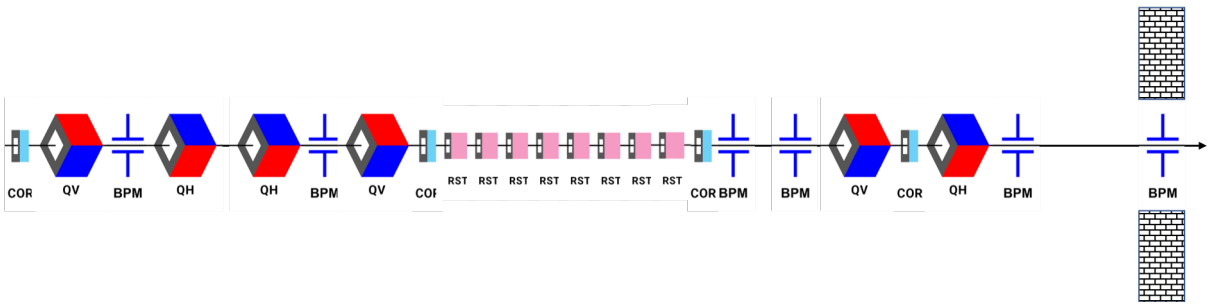

Figure 4: Diagram of the A2T, including the BPM positions, horizontal and vertically focusing quadrupole magnets (QH and QV, respectively), correctors (COR), the raster system (RST), and the separating wall aperture location.

In accelerator beam lines, quadrupole magnets control beam sizes by focusing the beam along the transverse planes. The quadrupoles are situated within the linac such that the design trajectory passes through their centers. Along this line, by construction, the quadrupole field is zero. A particle entering the quadrupole along the design trajectory will exit the quadrupole with its trajectory unaltered. A particle with some transverse offset with respect to the magnetic axis will undergo a deflection which is linearly proportional to the offset direction and amplitude [10]. The quadrupole acts as a magnetic focusing lens.

In this work, the magnetic fields are assumed to be dependent on the longitudinal displacement s such that the fields assume a constant value within the length of the magnets, while assuming a value of 0 in magnet free sections. This results in a piece-wise step-function distribution for the magnetic fields. In reality, fringe fields exist towards the ends of the fields, forming transitional regions between the field and field-free regions. The result of treating the fields as step-functions is referred to as the hard-edge model, and greatly simplifies the mathematical treatment of magnetic elements. [9].

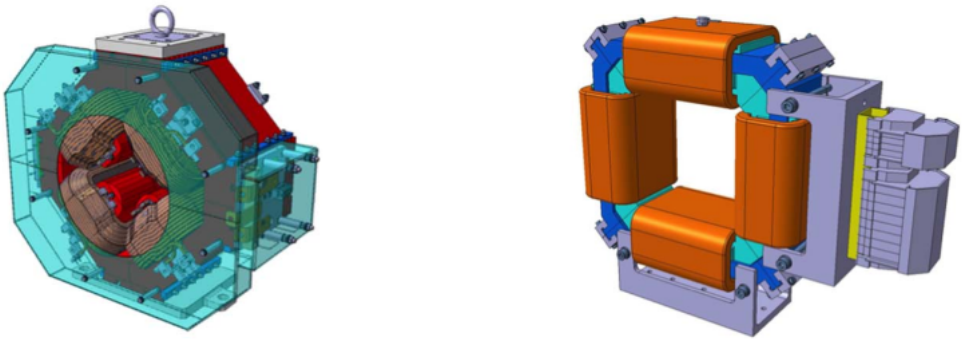

Figure 5: Perspective view of the quadrupole (left) and corrector (right) element designs.

The structure of the quadrupole and corrector magnets are presented above in Fig. 5. A result from Maxwell's equations [9] shows that quadrupole magnets focus only in one plane. Consider a positively charged particle moving through a quadrupole with some horizontal offset $x > 0$. It will experience a deflection toward the center, which is the focusing effect. A positively charged particle moving through that same quadrupole with a vertical offset $y > 0$ will instead be deflected upward, increasing the vertical offset and leading to defocusing. The geometry displayed in Fig. 5 shows an upright quadrupole, and rotating the quadrupole by 90° results in a reversal of the quadrupole polarity, and thereby swapping the focusing and defocusing planes [9].

The A2T is also equipped with horizontal and vertical correctors. Corrects are elements which deliver an angular kick du' to a charged particle without altering the transverse position u. The kick is applied such that the direction of the kick is perpendicular to both the particle trajectory and the field lines. Correctors generate dipole fields, with a horizontal corrector generating a field in the y direction and a vertical correcter in the x direction.

A Beam Position Monitor (BPM)s usually consists of a number of stacked capacitor plates. When a charged particle beam passes through a BPM, a voltage is induced in the element, and the signal is digitized. The transverse position u can then be measured.

2.3. Single-Particle Dynamics

Consider a charged particle moving in the s-direction with transverse coordinates (x, y), a velocity $\mathbf{v}$ and charge q. The force experienced by the particle when in the presence of an electromagnetic field is given by the Lorentz force equation:

$$\frac{\mathrm{d}\mathbf{p}}{\mathrm{dt}} = q\left(\mathbf{E} + \mathbf{v} \times \mathbf{B}\right) \tag{3}$$

where $\mathbf{E}$ and $\mathbf{B}$ are the external electric and magnetic fields, respectively. For high energy accelerators, the electric field component $\mathbf{E}$ in Eq. (3) is a result of accelerating structures. The A2T features no accelerating structures nor any elements acting on the longitudinal coordinate. This allows for the immediate setting of $\mathbf{E}$ to 0, and for taking v_s to be constant:

$$\frac{\mathrm{d}\mathbf{p}}{\mathrm{dt}} = q\left(\mathbf{v} \times \mathbf{B}\right) \quad . \tag{4}$$

Performing the cross product in Eq. (4) yields:

$$\frac{\mathrm{d}p_x}{\mathrm{dt}} = q(v_y B_s - v_s B_y), \quad \frac{\mathrm{d}p_y}{\mathrm{dt}} = q(v_s B_x - v_x B_s) \quad . \tag{5}$$

In most high energy sections of hadron linacs, and other high energy machines, it is uncommon to have elements which generate magnetic fields with B_s components. At the ESS, solenoids are used to focus the beam in the low energy sections of the linac, where they are still effective. For the high energy sections, such as the A2T, quadrupoles are more efficient for both focusing and transport [3]. Setting $B_s = 0$ and Taylor expanding B_x and B_y along s for small displacements in the transverse coordinates, while keeping only the linear terms:

$$\begin{aligned} B_x &= B_0 + \frac{\partial B_x}{\partial y} y + \frac{\partial B_x}{\partial x} x + \cancel{\frac{1}{2}\frac{\partial B}{\partial y} y^2} ... \\ B_y &= B_0 + \frac{\partial B_y}{\partial x} x + \frac{\partial B_y}{\partial y} y + \cancel{\frac{1}{2}\frac{\partial B}{\partial x} x^2} ... \end{aligned} \tag{6}$$

Assuming a planar accelerator with no dipole terms, we set $B_0 = 0$, and assuming independent and uncoupled motion in the transverse planes, we set $\frac{\partial B_x}{\partial x} = \frac{\partial B_y}{\partial y} = 0$ by construction.
Plugging Eqs. (1) and (6) into Eq. (4) yields:

$$\begin{aligned} x'' = -\frac{q}{p} B_y &= -\frac{q}{p}\left(\frac{\partial B_y}{\partial x} x\right) \\ x'' + \frac{q}{p}\frac{\partial B_y}{\partial x} x &= 0, \end{aligned} \tag{7}$$

and for the vertical plane

$$y'' - \frac{q}{p}\frac{\partial B_y}{\partial x} x = 0 \quad . \tag{8}$$

From the Maxwell equation in the absence of current density, $\boldsymbol{\nabla} \times \mathbf{B} = 0$, we have that $\frac{\partial B_y}{\partial x} = \frac{\partial B_x}{\partial y} = G$. Setting $K = \frac{q}{p} G$, we obtain the final equations of motion in both planes, which are known as Hill's equations [4]:

$$\begin{aligned} x'' + Kx &= 0, \\ y'' - Ky &= 0 \quad . \end{aligned} \tag{9}$$

2.4. Matrix Formalism

The focusing parameter K is a constant with a good approximation inside a quadrupole magnet and 0 everywhere else [4]. The transverse equations of motion derived above are second-order linear differential equations and their solutions can therefore be written in matrix form:

$$\begin{bmatrix} u \\ u' \end{bmatrix} = \begin{pmatrix} a & b \\ c & d \end{pmatrix} \begin{bmatrix} u_0 \\ u'_0 \end{bmatrix} \tag{10}$$

where $(u_0,\ u_0')$ are the initial position and angular divergence, respectively. The 2×2 matrix is designated the transfer matrix $\mathcal{M}$. The matrix formalism therefore allows us, given an initial condition, to obtain the particle amplitude and angular divergence at any point in the transfer line by calculating the product of the matrices of the elements in between two given points of interest. This transformation is then applied to the initial coordinates.

2.4.1. Quadrupole Transfer Map

Eq. (9) is the differential equation of a harmonic oscillator with a spring constant K. Using the Ansatz:

$$x(s) = \alpha_1 \cos(\omega s) + \alpha_2 \sin(\omega s) \tag{11}$$

Then, the first two derivatives are given by:

$$\begin{aligned} x'(s) &= -\alpha_1 \omega \sin(\omega s) + \alpha_2 \omega \cos(\omega s) \\ x''(s) &= -\alpha_1 \omega^2 \cos(\omega s) - \alpha_2 \omega^2 \sin(\omega s) \\ \Rightarrow x''(s) &= -\omega^2 x(s) \quad . \end{aligned} \tag{12}$$

A general solution for $\omega = \sqrt{K}$ is:

$$\begin{bmatrix} x \\ x' \end{bmatrix} = \begin{bmatrix} \alpha_1 \cos(\sqrt{K}s) & \alpha_2 \sin(\sqrt{K}s) \\ -\alpha_1 \sqrt{K} \sin(\sqrt{K}s) & \alpha_2 \sqrt{K} \cos(\sqrt{K}s) \end{bmatrix} \begin{bmatrix} x_0 \\ x_0' \end{bmatrix} \quad . \tag{13}$$

Applying the boundary conditions:

$$s = 0 \Longrightarrow \begin{cases} x(0) = x_0 \\ x'(0) = x_0' \end{cases} \rightarrow \begin{cases} x(0) = \alpha_1 x_0 \\ x'(0) = \alpha_2 \sqrt{K} x_0' \end{cases} \rightarrow \alpha_1 = 1, \quad \alpha_2 = \frac{1}{\sqrt{K}} \quad . \tag{14}$$

The final solution is then:

$$\mathcal{M}_Q = \begin{pmatrix} \cos(\sqrt{K}L) & \frac{1}{\sqrt{K}} \sin(\sqrt{K}L) \\ -\sqrt{K} \sin(\sqrt{K}L) & \cos(\sqrt{K}L) \end{pmatrix} \quad . \tag{15}$$

The solution Eq. (15) is valid for $K > 0$, so by a similar method, we seek an additional solution for the case $K < 0$ of the form:

$$x(s) = \alpha_1 \cosh \omega s + \alpha_2 \sinh \omega s, \quad \omega = \sqrt{|K|} \quad . \tag{16}$$

Applying the same initial conditions, the final solution is then:

$$\mathcal{M}_Q = \begin{pmatrix} \cosh(\sqrt{|K|}L) & \frac{1}{\sqrt{|K|}} \sinh(\sqrt{|K|}L) \\ -\sqrt{|K|} \sinh(\sqrt{|K|}L) & \cosh(\sqrt{|K|}L) \end{pmatrix} \quad . \tag{17}$$

Due to the geometry of the quadrupole magnetic field, as discussed in Sect. *2.2*, a quadrupole focusing along one transverse plane will automatically result in defocusing along the orthogonal transverse plane. This is reflected in the sign change of K, where $K < 0$ indicates a vertically focusing quadrupole and $K > 0$ a horizontally focusing quadrupole.

2.4.2. Drift Space Transfer Map

Drift sections contain no external fields, so obtaining the drift section transfer matrix is straight forward. Taking the limit of Eq. (15) as $K \to 0$ yields the transfer matrix for a drift section:

$$\mathcal{M}_D = \begin{pmatrix} 1 & L \\ 0 & 1 \end{pmatrix} \quad . \tag{18}$$

The action of a drift space on a particle's coordinates is given by:

$$\begin{pmatrix} 1 & L \\ 0 & 1 \end{pmatrix} \begin{pmatrix} u_0 \\ u_0' \end{pmatrix} = \begin{pmatrix} u_0 + u_0' L \\ u_0' \end{pmatrix} \quad . \tag{19}$$

2.4.3. Corrector Transfer Map

The kick strengths are given by:

$$dx' = -\frac{q}{p} BL, \quad dy' = \frac{q}{p} BL \quad . \tag{20}$$

Where q is the particle charge, p the momentum, B the magnetic gradient and L the element length. Correctors are not typically represented by transfer matrices, however, a mathematical "trick" will be used where we expand the dimensions of the transfer matrix from a 2×2 into a 3×3 matrix, and include the corrector contribution given in Eq. (20) as element r_{23} and write

$$\mathcal{M}_C = \begin{pmatrix} 1 & 0 & 0 \\ 0 & 1 & du' \\ 0 & 0 & 1 \end{pmatrix} \quad . \tag{21}$$

The corrector transfer matrix $\mathcal{M}$ has the following action on the coordinates of a particle propagating through it:

$$\begin{pmatrix} 1 & 0 & 0 \\ 0 & 1 & du' \\ 0 & 0 & 1 \end{pmatrix} \begin{bmatrix} u_0 \\ u_0' \\ 1 \end{bmatrix} = \begin{bmatrix} u_0 \\ u_0' + du' \\ 1 \end{bmatrix} \quad . \tag{22}$$

Since the corrector transfer matrix has a shape of 3×3, matrix algebra demands that we expand the other element's transfer matrices into 3×3 shapes. We then add an additional row and column consisting of 0 entries in the off-diagonals and 1 in the third diagonal entry. For example, the newly shaped drift section transfer matrix is given by:

$$\mathcal{M}_D = \begin{pmatrix} 1 & L & 0 \\ 0 & 1 & 0 \\ 0 & 0 & 1 \end{pmatrix} \quad . \tag{23}$$

2.4.4. Transfer Line Lattice

Through the use of the transfer matrices derived above, analysing the path of a charged particle through a beam line is straight forward. Given an arbitrary number of drift spaces, quadrupole magnets and correctors, we can represent a given sequence of elements by a series of transformation matrices $\mathcal{M}_i$. The beam line lattice is then simply equal to the product of the individual element transfer matrices.

For example, the action on a particle's coordinates propagating through the following

sequence; FODO, where F denotes a focusing quadrupole, O a drift space, and D a defocusing quadrupole, is given by

$$\mathcal{M}_{\text{total}} = \mathcal{M}_{\text{O}} \cdot \mathcal{M}_{\text{D}} \cdot \mathcal{M}_{\text{O}} \cdot \mathcal{M}_{\text{F}} \quad . \tag{24}$$

From Eq. (10), the particle coordinates are then transformed by the composite transfer map $\mathcal{M}_{\text{total}}$

$$\begin{pmatrix} u(s) \\ u'(s) \end{pmatrix} = \mathcal{M}_{\text{tot}}(s|s_0) \begin{pmatrix} u_0(s) \\ u_0'(s) \end{pmatrix} \quad . \tag{25}$$

where s_0 is the initial position at the focusing quadrupole, and s the position at the final drift space. The apparent reversal of the transfer map order is a necessary consequence of elementary matrix algebra.

The derived transfer maps for the three beam line elements feature no cross terms. This implies that motion in the transverse planes is effectively uncoupled and independent. This allows for the independent treatment of each plane, with the caveat that the normalised quadrupole gradients K must flip signs $K \to -K$ to reflect the change in focusing direction when changing transverse plane.

2.5. Beam Emittance and the Twiss Parameters

Propagating particles contained in the beam, which have slightly different initial conditions, through a transfer line lattice will result in a number of trajectories over which it is possible to define a beam envelope, see Fig 2. The envelope defines the beam distribution along the longitudinal direction on the transfer line and a good approximation for it in phase space is an ellipse, the area of which is given by ϵ. Given that we consider the transverse planes of motion independently, the parameter ϵ will be denoted ϵ_x and ϵ_y for the horizontal and vertical planes respectively.

The general equation for an ellipse centered at the origin in the horizontal (x, x') plane can be written as:

$$\gamma x^2 + 2\alpha x x' + \beta x'^2 = \mathcal{A}^2 \tag{26}$$

where the parameters γ, α and β are known as the Courant-Snyder parameters and together they determine the orientation of the phase space ellipse, as shown in Fig. 6.
The parameter β is a function obtained from Eq. (9) when assuming a solution of the form

$$x(s) = \mathcal{A}\sqrt{\beta(s)}\cos(\phi(s)), \tag{27}$$

while the parameters α and γ are functions of β:

$$\alpha \equiv -\frac{1}{2}\frac{d\beta}{ds}, \quad \gamma \equiv \frac{1+\alpha^2}{\beta} \quad . \tag{28}$$

At this point, we separate single- and multiple-particle dynamics. $\mathcal{A}$ describes the amplitude dependence on initial conditions for a single particle. $\mathcal{A}$ is constant along the transfer line but each individual particle has a different value for it. The emittance ϵ is related to $\mathcal{A}$ by $\epsilon = \mathcal{A}^2$.

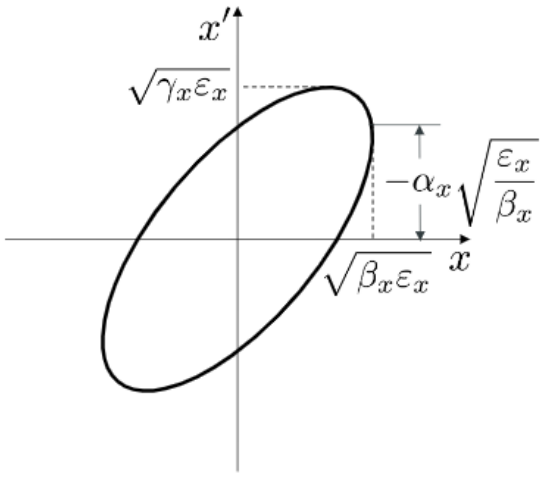

Figure 6: Horizontal phase-space ellipse described by Eq. (26) including relations for several important points along the ellipse.

For a collection of particles at a position s along the beam line, it is possible to define an area which will enclose most of the particles. For example, 68.2% or 1σ assuming a Gaussian distribution. This area carries the special significance of the beam emittance, and is equal to the area enclosed by the phase-space ellipse ϵ. The beam emittance is a constant of motion.
The function $\beta(s)$ describes the amplitude dependence of the particle motion on the lattice, and it is has a direct dependence on the quadrupole strengths. Its value will therefore vary along the transfer line.

2.6. Space Charge

Particle motion in the linac depends not only on applied external fields, but also on fields induced by the Coulomb interactions of charged particles within the beam. As the beam current increases, these Coulomb interactions become increasingly important. The charged particles produce mutually repulsive electric fields and also attractive magnetic fields. The resulting electric and magnetic fields generate Lorentz forces which act in opposition to the net focusing given by the lattice [1]. Consider a uniform, cylindrical beam with N particles per unit length, and with a radius r. Charged particles within $(a < r)$ the beam will experience a net space charge force given by:

$$F(a) = \frac{q^2 N}{2\pi\epsilon_0 \gamma^2} \frac{a}{r^2} \quad . \tag{29}$$

The repulsion force present in high density beams is called space charge. Space charge is an important effect for low energy beams. The forces experienced by charged particles due to space charge Lorentz forces are inversely proportional to the Lorentz factor squared, shown in Eq. (29). For ultra-relativistic beams, the Lorentz factor is large ($\gamma \gg 1$), and space charge effects can then be considered negligible [1, 7].

3. Software and Methods

This section briefly summarises the software used and the methods implemented to calculate the required corrector strengths and the beam waist position.

3.1. Python

A Python program was written in order to simulate the beam centroid trajectories through a simplified model of the ESS A2T beam line. Given the Twiss parameters at the aperture located at the end of the A2T and the emittance, the program paints the phase space ellipses in the (x, x') and (y, y') planes and plots a number of points along them. These points are then back-propagated through the beam line to the transverse position $(0, 0)$ at the beginning of the beam line. The kick values for the correctors in the beam line are calculated, as explained in the section 3.3, and finally the particles are then sent through the beam line with the calculated corrector strengths. These trajectories are then plotted.

The Python code in its entirety is found in the Appendices.

3.2. OpenXAL

OpenXAL [5] is an open-source development environment used for creating accelerator physics applications and scripts [2], which is used in the control room at the ESS in order to develop various applications. Simulations performed in OpenXAL include additional effects such as space charge and will act as benchmarks against the simulation results obtained from the Python code.

3.3. Corrector Solving Method

In order to place the beam centroid over the calculated ellipses on the (x, x') and (y, y') planes at the wall the beam has to be displaced along the A2T. The corrector strengths used to kick the beam causing those displacements need to be pre-calculated. In this section the general method used to find the strength values is outlined.

From Eq. (26) and a known set of Courant-Snyder parameters, a phase-space plot is generated at the end of the beam line. From this, a set of i equidistant points (u_i, u_i') which lie along the ellipse given by Eq. (26) is obtained. These points are then back-propagated through the reversed beam line R_T^* to the origin:

$$R_T^*(ST_k) \begin{pmatrix} u_i \\ u_i' \end{pmatrix} = \begin{pmatrix} u_0 \\ u_0' \end{pmatrix} = \begin{pmatrix} 0 \\ 0 \end{pmatrix} \tag{30}$$

where (u_i, u_i') and (u_0, u_0') are the final and initial particle positions respectively in each transverse plane. From this relation, we obtain a system of equations of the form:

$$\begin{cases} aST_1 + bST_2 + cST_3 + dST_4 = 0 \\ eST_1 + fST_2 + gST_3 + hST_4 = 0 \end{cases} \tag{31}$$

The corrector strength values ST_i are calculated using a linear equation system solver module in Python. As there are 4 distinct correctors and only 2 equations, the system is under-determined and no independent solution exists. To alleviate this, a variety of couplings for the correctors are simulated. Coupling here entails, for example, that the first and third correctors have some multiple of the same strength value, as do the second and fourth correctors, respectively. The coupling scheme that minimises the maximum

corrector kick strength is considered desirable.

As an example, we consider the case $ST_2 = \alpha ST_1, \quad ST_4 = \beta ST_3$. We then solve:

$$\begin{cases} (a + b\alpha)ST_1 + (c + d\beta)ST_3 = 0 \\ (e + f\alpha)ST_1 + (g + h\beta)ST_3 = 0 \quad . \end{cases} \tag{32}$$

For each initial condition i we obtain a solution for Eq. (32), which is in turn plugged into the beam line and propagated. The trajectories of these particles are then plotted.

3.4. Trajectory Waist Position Determination

The collection of centroid trajectories created with the corrector strengths calculated in Sect. *3.3* bear little resemblance to the envelope at the start of the A2T (see Sect. *4.3*), but those correctors will force them to match the envelope at the separating wall. Since there are no external fields between the last quadrupole and the wall, and assuming space charge effects are negligible, the trajectories and the envelope behaviour should also match in that entire region. Therefore, it should be possible to estimate the waist position of the trajectory envelope, which in turn should coincide with the waist position of the beam envelope, using the BPMs located between the last quadrupole and the wall in the A2T.

The final two BPMs are located at the positions 19.6 m and 22.6 m, respectively. For each beam centroid trajectory, the transverse positions u are measured at each BPM. A line is then traced between them. A straight line is a good fit as these positions are located after the final quad, and are therefore propagating through a drift space. For each point s between the two BPMs, the maximum position value u among all trajectories is measured and plotted, forming an envelope curve. The minimum of this curve is the waist position.

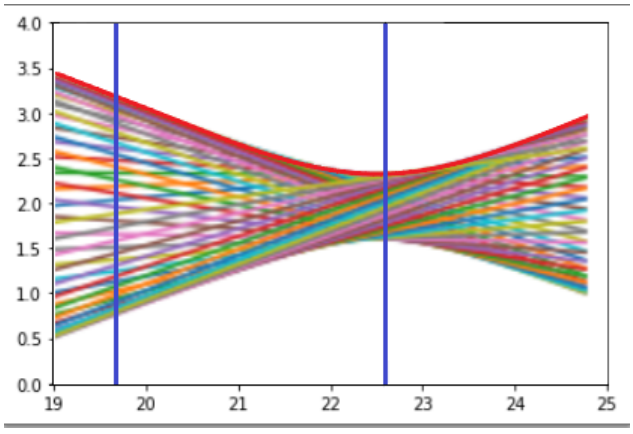

Figure 7: Illustrative example of waist reconstruction from BPM position measurements. The blue lines indicate BPM positions. The various coloured lines are linear fits between measured positions at the BPMs. The red line indicates the maximum position values u for each point along s.

4. Results

The first part of this section deals with space charge effects, and their impact on this thesis' results, before moving on to the main results of the project; determination of corrector strength values the beam waist location. Finally, lattice errors are considered and examined.

4.1. Effects of Space Charge

In this work, beam centroids are plotted in order to infer beam waist positions, which are beam envelope properties. Centroids do not experience space charge effects, while the beam envelope is indeed affected by space charge. This could then potentially lead to mismatched beam waist positions for the envelope and centroid trajectories.

A qualitative analysis of the ratio between the quadrupole magnet force and the force generated by space charge effects is therefore necessary, as the beam in the A2T can not be considered ultra-relativistic ($\gamma \approx 3$).

From Eq. (29), assuming a beam of radius r, let $a = x,\ x > r$, and for the space charge force we obtain:

$$F_{SC} = \frac{q^2 N}{2\pi\epsilon_0\gamma^2}\frac{x}{r^2} \quad . \tag{33}$$

The strength of the quadrupole is given by Eq. (3). Performing the cross product yields:

$$F_{quad} = qv_s\left(\frac{\partial B_x}{\partial y}y - \frac{\partial B_y}{\partial x}x\right) \quad . \tag{34}$$

Having defined $G = \frac{\partial B_x}{\partial y} = \frac{\partial B_y}{\partial x}$ and since the particle is at $a = x \implies y = 0$, then we have:

$$F_{quad} = -qv_sGx = -q\beta cGx \quad . \tag{35}$$

Assuming an average gradient of $G \approx 1$, an average beam size of $r \approx 2\,\text{mm}$, a beam charge of $2 \cdot 10^{-8}$ C/m, a normalised velocity $\beta = 0.94$ and a Lorentz factor $\gamma \approx 3$, taking the quotient of the two forces yields:

$$\left|\frac{F_{SC}}{F_{quad}}\right| = \frac{qN}{2\pi\epsilon_0\beta c\gamma^2 G}\frac{1}{r^2} \approx 10^{-2} \quad . \tag{36}$$

Space charge effects can therefore safely be neglected. This is further strengthened by Fig. 8 below, which shows an OpenXAL[5] simulation where the evolution of the 1σ beam envelope is plotted in both transverse planes for zero current and at a nominal 62.5 mA current. The first case implies no space charge effects, and is practically indistinguishable from the nominal current plot. This confirms our decision to neglect space charge.

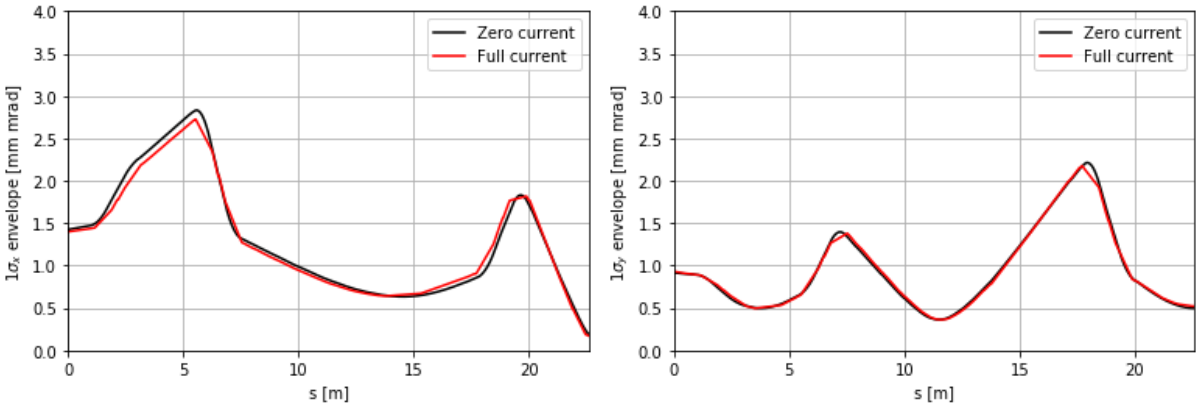

Figure 8: Benchmark simulation demonstrating the 1σ envelope evolution through the beam line in both the x and y plane, with and without space charge effects represented by full (red) and zero (black) current envelope lines, respectively.

4.2. Courant-Snyder Parameters and Beam Emittance

The given Courant-Snyder parameters, as well as the assumed beam emittance, which are used throughout the simulations presented in the following section, are shown below in Table 1:

Table 1: Courant-Snyder parameter values at the aperture position and beam emittance used to plot phase space ellipses in Fig. (9)

Parameters	**Horizontal**	**Vertical**
α	-0.0165	-0.0222
β [m]	0.2640	2.115
ϵ [mm mrad]	1.0798×10^{-7}	1.2302×10^{-7}

Plugging these values into Eq. (26) produces the following phase space plots at wall aperture (where the last BPM is located):

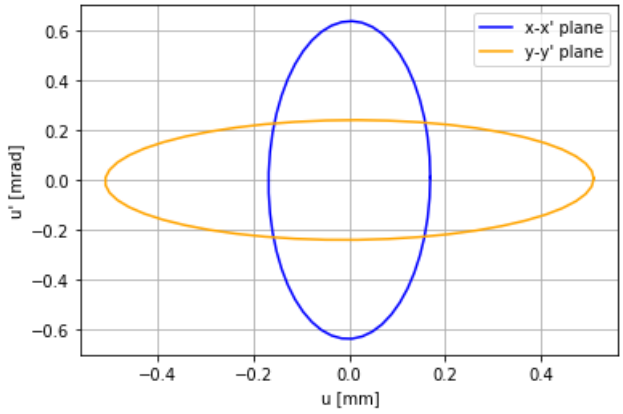

Figure 9: Phase space ellipses defined by the Courant-Snyder parameters at the aperture.

For the calculation of the correctors strengths show in the next session, 50 equidistant points lying along each of these ellipses are then back propagated through the beam line to the beginning of the A2T with the initial condition $(u, u') = (0, 0)$ for the beam centroid.

4.3. Corrector Strength Simulations

There are 4 correctors in the A2T, and in this thesis they are modeled as thin lenses. In physical accelerators, correctors have a non-zero length, and the angular kick du' will be applied along the length of the element. This model instead assumes that the full angular kick du' is applied at the center of the corrector. This allows for a much simpler implementation of the correctors.

A vital part of this project was to demonstrate that the corrector strengths can be accurately calculated, within a margin of error, and that these corrector strengths will yield correct trajectories which coincide at the waist. The calculated strengths must also lie beneath the limit of 1.08 mrad due to power supply constraints.

For each transverse plane, the correctors were coupled according to three distinct schemes designated cases 1 through 3. The schemes are presented below in Table 2 and the results for each coupling scheme are plotted in Fig. 10. They show that, regardless of the chosen coupling scheme, the calculated strengths are consistently below the limit of 1.08 mrad for both transverse planes. The cases featuring the lowest maximum corrector strengths are considered the most desirable, and that is case 2 for the (x, x') plane, and case 3 for the (y, y') plane. These two cases are then used in the following simulation sections.

Table 2: Corrector coupling schemes of each case along with the associated max correcter strength value.

Case	**1st Coupling**	**2nd Coupling**	**Max. Corrector Strength [mrad]**	
			(x, x')	(y, y')
1	ST4 : ST1	ST2 : ST3	0.131	0.266
2	ST4 : ST3	ST2 : ST1	0.056	0.457
3	ST4 : ST2	ST1 : ST3	0.076	0.184

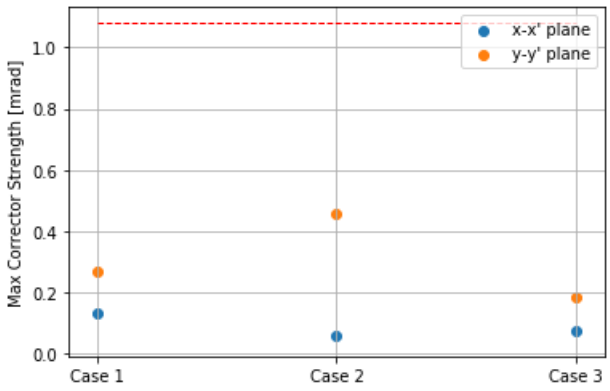

Figure 10: Comparison of the maximum corrector strengths of the various coupling schemes in each plane. The red dotted line represents the physical limit for the maximum corrector strength value.

4.4. Trajectory Simulation and Waist Position Determination

At the position $s = 22.6$ m, the beam passes through the aperture wall separating the A2T from the target. The separating wall represents an aperture restriction, and as such, the proton beam has a waist at that position by design.

The envelope of the beam is proportional to the beam size at each location in the beam line according to the relation $\sigma = \sqrt{\beta\epsilon}$, as shown Fig. 6, and is nothing more than a measurement of the spread of a collection of many single-particle trajectories. A single centroid trajectory evolves as a single-particle following Eq. (27), and thus a collection of centroid trajectories, given that the boundaries conditions are correctly set, should emulate the beam envelope and present a waist at the same position s.

It was shown in Sect. *4.3* that space charge effects are negligible for the beam in the A2T. Using the method detailed in Sect. *3.4*, we determine the trajectory envelope waist position between the last two BPMs in the A2T. We expect this position to coincide with the beam envelope waist position. This is demonstrated in the following trajectory plots shown in Fig. 11 for the design lattice settings, where the beam forms a waist at the final BPM position. The coincident beam waists in Fig. 11 demonstrate that the assumptions and approximations used in this work are valid and correct.

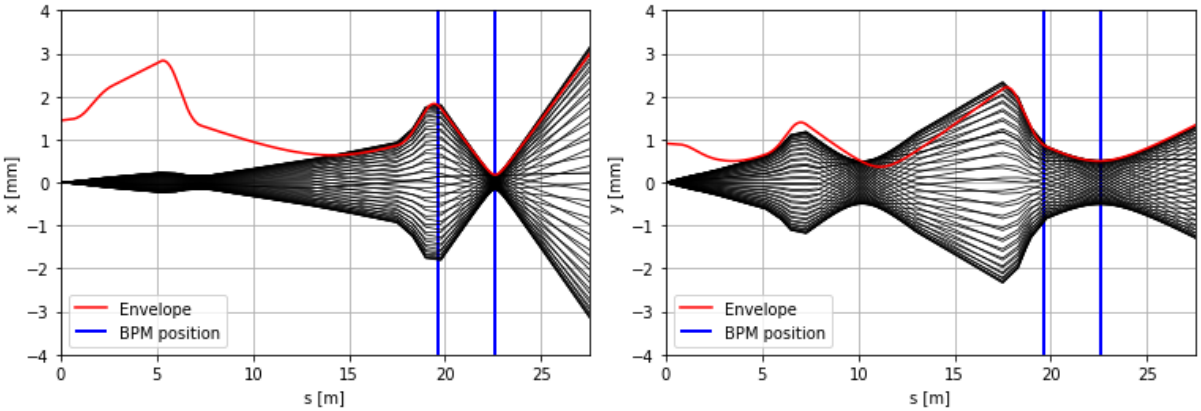

Figure 11: Trajectory plots for the select correcter couplings from section *4.3* showing coincident waist formation of beam centroid trajectories and beam envelope.

4.5. Lattice Error Study

This section examines the effect of errors in the transfer line lattice. Two different error sources are considered. The first method is by significantly altering the focusing strength of one of the last quads in the beam line, causing a visible shift in the waist position. The second method is to introduce small amounts of variation in each individual quadrupole magnet strength in the A2T. The effects on the trajectories are then analysed.

The results from the first method are plotted below in Fig. 12 and 13. The location of the beam waist position is determined entirely by the β function, and by extension, the beam line lattice. The ability to identify the beam waist position in the presence of significant error in the beam line lattice is an important result as that implies the method is adequate for real beam line lattices, and not just for ideal cases.

In Fig. 12, a 5% error is introduced to the normalized gradient K of the sixth quadrupole, and this results in a longitudinal shift of the waist from $s = 22.60\,\mathrm{m}$ to $s = 22.03\,\mathrm{m}$ in the (x, x') plane and $s = 22.74\,\mathrm{m}$ in the (y, y') plane. The opposing directions of these two shifts is a consequence of the polarity reversal in the quadrupole gradients between the transverse planes. A stronger final quadrupole leads to the formation of a premature

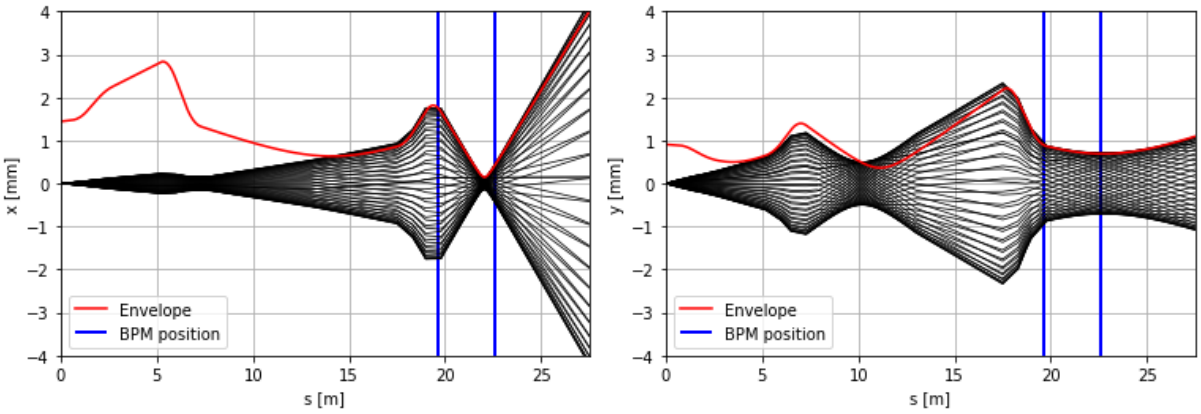

Figure 12: Longitudinal shifting of waist position due to a 5% error in the sixth and final quadrupole magnet strength.

waist while a weaker final quadrupole causes a delayed waist to form.

A similar situation is seen in Fig. 13, where a 5% error has been induced in the fifth quadrupole. In the (x, x') plane, the waist is shifted to $s = 22.37\,\text{m}$. In the (y, y') plane, the waist is shifted to $s = 19.79\,\text{m}$. The vertical plane in Fig. 13 shows the largest deviation in waist position estimation when compared to the envelope values. This is possibly due to the fact that the waist in this case is very close to the last quadrupole position, thus pushing our initial assumptions to the limit.

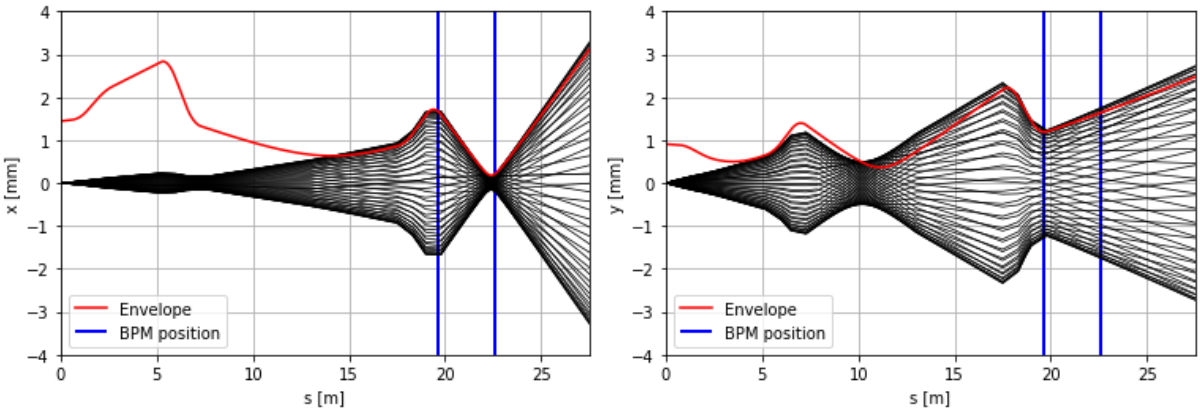

Figure 13: Longitudinal shifting of waist position due to a 5% error in the fifth quadrupole magnet strength.

The second method for introducing errors to the beam line lattice is by implementing random noise in the quadrupole magnets throughout the beam line. The error values are generated by a standard implementation of Gaussian noise, where a σ value is chosen and then multiplied by a random number between 0 and 1, and then by a random choice of 1 or -1.

The particle trajectories are plotted along with the envelope of the design beam line lattice as a comparison. Amplitude variation on the gradients of of 5% and 10%, respectively, are plotted in Fig. 15 below.

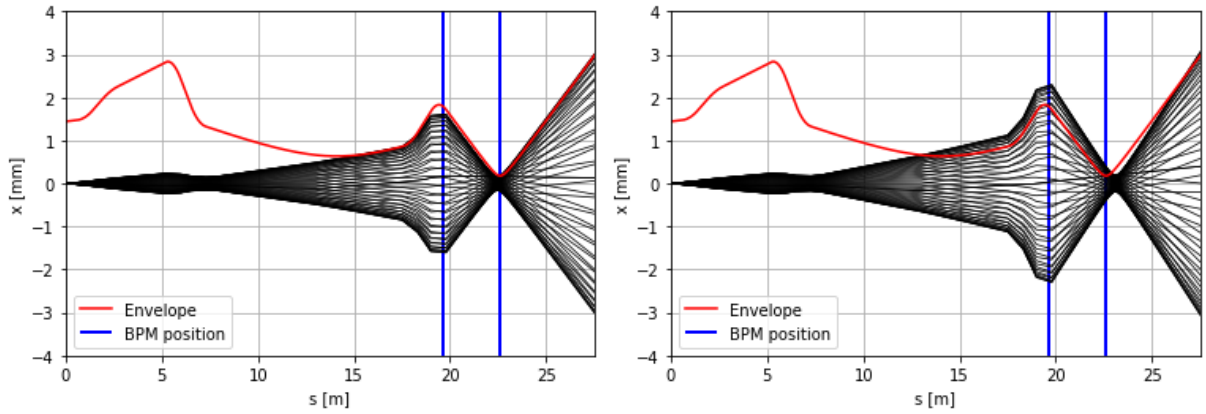

Figure 14: Longitudinal shift of waist position in the (x, x') plane due to a 5% (left) and 10% (right) noise effect in all six quadrupole magnet strengths.

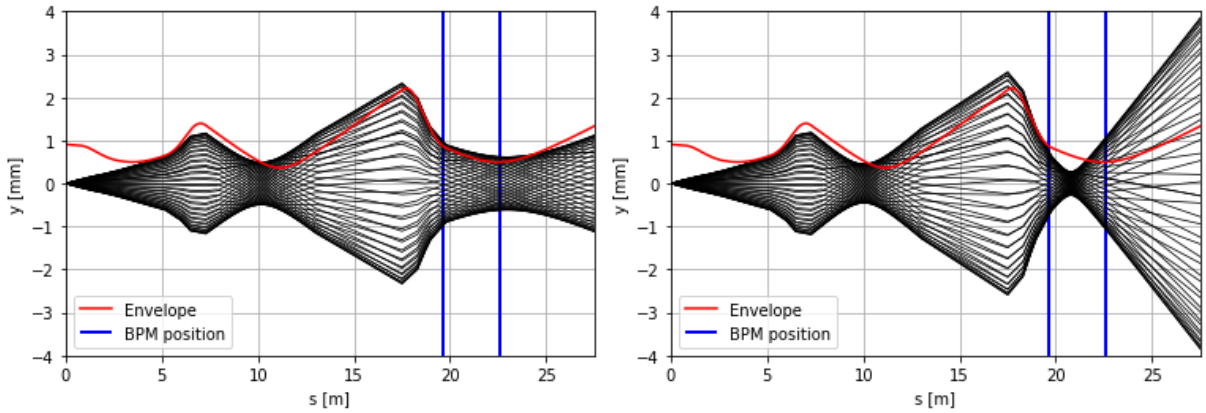

Figure 15: Longitudinal shift of waist position in the (y, y') plane due to a 5% (left) and 10% (right) noise effect in all six quadrupole magnet strengths.

A variation of 5% resulted in minor shifts of the waist position from $s = 22.6\,\text{m}$ to $22.33\,\text{m}$ in the horizontal plane and to $22.70\,\text{m}$ in the vertical. For the 10% variation simulation, waist positions shifted to $22.24\,\text{m}$ in the horizontal plane and to $20.46\,\text{m}$ in the vertical. The directions of the observed shifts depend on the random choice of -1 or 1, and so are not indicative of successive iterations. Only the magnitude of the observed shift is therefore relevant.

Table 3 provides a summary of the beam waist positions obtained both from the waist determination method and from the benchmark simulations for Figs. 11, 12 and 13. It should be noted that the plotted benchmark envelopes for the variational lattice are those of the design lattice simply to act as a visual guide. Table 3 therefore only includes the waist determination method beam waist positions.

Table 3: Beam waist positions along with their beam envelope benchmark values.

Case	**Waist longitudinal positions [m]**			
	from Trajectory		**from Envelope**	
	Horizontal	Vertical	Horizontal	Vertical
Design Lattice	22.58	22.47	22.61	22.47
5% error in 5^{th} quad.	22.37	19.79	22.42	19.65
5% error in 6^{th} quad	22.03	22.74	22.08	22.71
5% error in all quads	22.33	22.70	-	-
10% error in all quads	22.24	20.46	-	-

5. Conclusions and Outlook

The goal of this thesis was to establish the viability of determining the proton beam waist position using a set of known Courant-Snyder parameters at the aperture, a known beam emittance ϵ and the main diagnostic tools available at the end of the A2T, those being two BPMs. A simplified version of the A2T beam line was constructed in Python and several simulations were performed.

The corrector strengths calculated in order to create the desired trajectories, were far below the the maximum value limit, regardless of the case, and produced good results. The coupling method used also allows only a subset of possible solutions and a natural extension would be to allows different corrector combinations or use a more advance method to solve the set of equations for the correctors.

The results from the waist determination method detailed in section *3.4* were compared to envelope waist positions obtained from benchmark OpenXAL[5] simulations. The method determined waist positions in the horizontal plane with deviations on the order of a few centimeters.
The effect of error propagation in the quadrupole magnets was examined using two distinct methods. For the first method, introducing significant errors in the final two quadrupoles resulted in longitudinally shifted waist formations. This is an unlikely scenario as a 5% error in the normalized gradient of a critical quadrupole magnet would be immediately noticeable during commissioning. It does however serve as an indicator of the viability of the method in the presence of significant errors.

When variations were introduced in the magnetic gradient of all six quadrupole magnets, similar results to the previous simulations were seen. A 5% variation produced trajectories which were almost identical to the design lattice trajectories. A 10% variation produced significantly larger waist position shifts as expected. This indicates that beam waist positions are still able to be reliably determined using the novel method when significant fluctuations in the magnetic element's strengths are present in the lattice.

This work could be further extended by extending the error study to include; the measurement errors of the BPMs, errors in correctors kick applications and also in the beam's initial position. Another effect that is worth studying is determining the minimum shift in waist position that we are able to measure.

We have examined the viability of using BPMs in order to measure beam parameters other than position. We have demonstrated that the method accurately and reliably locates the proton beam waist positions in both ideal beam lines and in beam lines featuring significant quadrupole errors. This means that facilities such as the ESS can further optimise their usage of BPMs as diagnostic tools.

References

[1] M Ferrario, M Migliorati, and L Palumbo. "Space Charge Effects". In: (2014). DOI: 10.5170/CERN-2014-009.331. URL: https://cds.cern.ch/record/1982426 (visited on 05/17/2021).

[2] J. Galambos et al. "XAL Application Programming Structure". In: *Proceedings of the 2005 Particle Accelerator Conference*. 2005 Particle Accelerator Conference. Knoxville, TN, USA: IEEE, 2005, pp. 79–83. ISBN: 978-0-7803-8859-8. DOI: 10.1109/PAC.2005.1590365. URL: http://ieeexplore.ieee.org/document/1590365/ (visited on 05/17/2021).

[3] Roland Garoby. "The European Spallation Source Design". In: *Physica Scripta* 93.1 (Dec. 1, 2018). In collab. with A Vergara et al., p. 014001. ISSN: 0031-8949, 1402-4896. DOI: 10.1088/1402-4896/aa9bff. URL: https://iopscience.iop.org/article/10.1088/1402-4896/aa9bff (visited on 05/10/2021).

[4] S. Y. Lee. *Accelerator physics*. 2nd ed. Hackensack, N.J: World Scientific, 2004. 575 pp. ISBN: 978-981-256-182-4 978-981-256-200-5.

[5] *Open XAL*. URL: http://openxal.github.io/ (visited on 05/17/2021).

[6] Rüdiger Paschotta. *Field guide to lasers*. SPIE field guides v. FG12. Bellingham, Wash: SPIE Press, 2008. 139 pp. ISBN: 978-0-8194-6961-8.

[7] S. X. Peng et al. "Study on Space Charge Compensation of Low Energy High Intensity Ion Beam in Peking University". In: *HB2016 in Malmö, Sweden*. HB2016. State Key Laboratory of Nuclear Physics and Technology & Institute of Heavy Ion Physics, School of Physics, Peking University, Beijing, China, University of Chinese Academy of Sciences, Beijing, China, 2016.

[8] M. Reiser. *Theory and design of charged particle beams*. Wiley series in beam physics and accelerator technology. New York: Wiley, 1994. 607 pp. ISBN: 978-0-471-30616-0.

[9] Helmut Wiedemann. *Particle Accelerator Physics I: Basic Principles and Linear Beam Dynamics*. OCLC: 851375634. Berlin, Heidelberg: Springer Berlin Heidelberg, 1999. ISBN: 978-3-662-03827-7. URL: https://doi.org/10.1007/978-3-662-03827-7 (visited on 05/10/2021).

[10] Andrzej Wolski. *Beam dynamics in high energy particle accelerators*. OCLC: ocn870563766. London : Singapore ; Hackensack, NJ: Imperial College Press ; Distributed by World Scientific, 2014. 591 pp. ISBN: 978-1-78326-277-9.

Appendices

A. Python code

```
import numpy as np
import matplotlib.pyplot as plt
import sympy
import random

### Courant-Snyder Parameters###

### x - x' Plane ###
#alpha = -0.0165
#beta = 0.2640

### y - y' Plane ###
alpha = -0.0222
beta = 2.115

gamma = (1 + alpha**2)/beta

epsilon_x = (0.3194*10**(-6))/2.958
epsilon_y = (0.3639*10**(-6))/2.958

########## Element Transfer Maps ##########
### Drift Section ###
def driftscn(L):
    return [(sympy.Matrix([[1, L, 0], [0, 1, 0], [0, 0, 1]]), L)]

##### Quadrupole Magnets #####
def Quad(l, k):
    if k >= 0:
        M = [(sympy.Matrix([[np.cos(np.sqrt(k)*l), np.sin(np.sqrt(k)*l)/
   np.sqrt(k), 0],
            [-np.sqrt(k)*np.sin(np.sqrt(k)*l), np.cos(np.sqrt(k)*l),
   0], [0, 0 , 1]]),l)]
    elif k < 0:
        M = [(sympy.Matrix([[np.cosh(np.sqrt(abs(k))*l), np.sinh(np.sqrt
   (abs(k))*l)/np.sqrt(abs(k)), 0],
            [np.sqrt(abs(k))*np.sinh(np.sqrt(abs(k))*l), np.cosh(np.
   sqrt(abs(k))*l), 0], [0, 0, 1]]),l)]
    return M

### Corrector Magnets ###
def steerer(dx):
    return [(sympy.Matrix([[1, 0, 0], [0, 1, dx], [0, 0, 1]]), 0)]

### One-Turn Function
def oneturn(beamline):
    M = np.eye(3)
    l = 0
    for i in beamline:
        M=i[0] @ M
        l += i[1]
    return [(M, l)]

### Trajectory Plotting Function ###
```

```
50 def Trajectory(x, xp, beamline,long_pos, waist):
51     L_2 = 1
52     particle = [(np.array([[x], [xp], [1]]), 0)]
53     beamline = beamline + 5*driftscn(1)
54     for i in beamline:
55         particle.append((i[0] @ particle[-1][0], particle[-1][1] + i[1])
       )
56     plt.plot ([i[1] for i in particle], [i[0][0]*1000 for i in particle
       ], color='black', linewidth=0.75)#, label='Trajectories' if i[1] == 0
        else "")
57     plt.grid (True)
58     plt.xlabel('s [m]')
59     plt.ylabel('y [mm]')
60     plt.ylim(-4, 4)
61     plt.xlim(0, 27.5)
62     BPM93 = float(particle[100][0][0])
63     BPM94 = float(particle[110][0][0])
64     #waist in X
65     z = np.polyfit([19.79,22.6],[BPM93, BPM94],1)
66     p=np.poly1d(z)
67     for j in range(len(long_pos)):
68         if waist[j]<p(long_pos[j]):
69             waist[j]=p(long_pos[j])
70     return waist
71 
72 def beamline_gen(ST1, ST2, ST3, ST4, x, xp, k_list):
73     xf = np.array([[x], [xp], [1]])
74     ##### Parameter choices #####
75     L = 1
76     LQ = 0.8
77     beamline = steerer(ST1) + 10*driftscn((0.59*L)/10) + Quad(LQ, k_list
       [0]) + 10*driftscn((0.5*L)/10) + Quad(LQ, k_list[1]) + 10*driftscn
       ((2.5*L)/10) + Quad(LQ, k_list[2]) + 10*driftscn((0.5*L)/10) + Quad(
       LQ, k_list[3]) + 10*driftscn((0.55*L)/10) + steerer(ST2) + 10*
       driftscn((5.16*L)/10) + steerer(ST3) + 10*driftscn((4.501*L)/10) +
       Quad(LQ, k_list[4]) + 10*driftscn((0.415*L)/10) + steerer(ST4) + 10*
       driftscn((0.275*L)/10) + Quad(LQ, k_list[5]) + 10*driftscn((2.82*L)
       /10)
78     r_beamline = beamline[::-1]
79     OTM = oneturn(r_beamline)
80     M = OTM[0][0] @ xf
81     return M
82 
83 ############ Steerer solving #############
84 def circle_plot(alpha, beta, epsilon, n):
85     r = np.sqrt(epsilon*beta)
86     t = np.linspace(0, 2*np.pi,n)
87     x = r*np.cos(t)
88     y = r*np.sin(t)
89     xp = (y - alpha*x)/beta
90     fig, ax = plt.subplots(1)
91     ax.plot(x*1000, xp*1000)
92     plt.xlabel('u [mm]')
93     plt.ylabel("u' [mrad]")
94     plt.grid(True)
95     plt.show()
96     return [x, xp]
97 
```

```
98  def beamline_final(x, xp, plane='y'):
99      ST1, ST2, ST3, ST4 = sympy.symbols('ST1, ST2, ST3, ST4')
100     k = 1
101     xi = np.array([[0], [0], [1]])
102     ST_list = []
103     ST_max = []
104     ST_maxmax = []
105     points = []
106 
107     ##### Element Length Parameters #####
108     L = 1
109     LQ = 0.8 # Quadrupole
110 
111     ##### Quadrupole Gradients #####
112     B0 = np.array([-3.40464,1.57147,6.0093,-7.877,-6.96187,8.56988])
113     p0 = 2775054522.1322517*1e-9
114     brho = 3.3357*p0
115 
116     if plane == 'x':
117         k_list = B0/brho
118     elif plane =='y':
119         k_list = -1*B0/brho
120 
121     n_list=[]
122     long_pos=np.arange(19.79,25.6,0.001)
123     waist=np.zeros(len(long_pos))
124 
125     ##### Variational Quadrupole Gradients #####
126     for i in k_list:
127         noiseSigma = 0.05*i
128         noise = i + random.choice([-1,1])*noiseSigma*np.random.rand(1,1)
129         n_list.append(noise[0][0])
130 
131     for i in range(len(x)):
132         R = beamline_gen(ST1, ST2, ST3, ST4, x[i], -xp[i],k_list)
133         eq1 = sympy.Eq(R[0].subs({ST1:ST3, ST4:ST2}), 0)
134         eq2 = sympy.Eq(R[1].subs({ST1:ST3, ST4:ST2}), 0)
135         result = sympy.solve([eq1, eq2], (ST3, ST2))
136         ST2_k, ST3_k = result[ST2], result[ST3]
137         ST4_k, ST1_k = ST2_k, ST3_k
138 
139         # Lattice choice: pick 1 #
140         # Design lattice #
141         final_lattice = steerer(ST1_k) + 10*driftscn((0.59*L)/10) + Quad
    (LQ, k_list[0]) + 10*driftscn((0.5*L)/10) + Quad(LQ, k_list[1]) + 10*
    driftscn((2.5*L)/10) + Quad(LQ, k_list[2]) + 10*driftscn((0.5*L)/10)
    + Quad(LQ, k_list[3]) + 10*driftscn((0.55*L)/10) + steerer(ST2_k) +
    10*driftscn((5.16*L)/10) + steerer(ST3_k) + 10*driftscn((4.501*L)/10)
     + Quad(LQ, k_list[4]) + 10*driftscn((0.415*L)/10) + steerer(ST4_k) +
     10*driftscn((0.275*L)/10) + Quad(LQ, k_list[5]) + 10*driftscn((2.82*
    L)/10)
142         # Lattice with variations #
143         final_lattice = steerer(ST1_k) + 10*driftscn((0.59*L)/10) + Quad
    (LQ, n_list[0]) + 10*driftscn((0.5*L)/10) + Quad(LQ, n_list[1]) + 10*
    driftscn((2.5*L)/10) + Quad(LQ, n_list[2]) + 10*driftscn((0.5*L)/10)
    + Quad(LQ, n_list[3]) + 10*driftscn((0.55*L)/10) + steerer(ST2_k) +
    10*driftscn((5.16*L)/10) + steerer(ST3_k) + 10*driftscn((4.501*L)/10)
     + Quad(LQ, n_list[4]) + 10*driftscn((0.415*L)/10) + steerer(ST4_k) +
```

```
    10*driftscn((0.275*L)/10) + Quad(LQ, n_list[5]) + 10*driftscn((2.82*L)/10)
144
145         Trajectory(0, 0, final_lattice,long_pos, waist)
146         OTM = oneturn(final_lattice)
147         M = OTM[0][0] @ xi
148         points.append(M)
149         ST_list.append([(np.array([[ST1_k, ST2_k], [ST3_k, ST4_k]]))])
150         ST_max.append(max(abs(ST1_k), abs(ST2_k), abs(ST3_k), abs(ST4_k))
151         X = np.array([x[i], xp[i]])
152         k += 1
153     ST_maxmax.append(max(ST_max))
154     print(ST_maxmax)
155     ind = np.where(waist==np.min(waist))[0]
156     print('waist position = ',long_pos[ind[0]])
157     plt.axvline(x=long_pos[ind[0]], label='Waist position')
158     return M, X, ST_list, ST_maxmax, final_lattice, points #, S_list
159
160 x, xp = circle_plot(alpha,beta, epsilon_y, 50)
161 M, X, ST_list, ST_maxmax, final_lattice, points = beamline_final(x, xp)
162
163 ### Loading envelope data and plotting ###
164 envelope_plot=np.loadtxt('envelopes(1).txt')
165 plt.plot(envelope_plot[0], envelope_plot[2], label='Envelope', color='red')
166 plt.vlines(x=22.6, ymin=-5, ymax=5, linewidth=2, color='b', linestyle='-', label='BPM position')
167 plt.vlines(x=19.6, ymin=-5, ymax=5, linewidth=2, color='b', linestyle='-')
168 plt.legend(loc='lower left')
```

B. 2021 International Beam Diagnostics Conference (IBIC) Abstract

Determination of the beam transverse waist position using BPMs readings at ESS

G. Fahlström, N. Milas, R. Miyamoto and T. Shea

The European Spallation Source (ESS), currently under construction in Lund, Sweden, will be the world's most powerful neutron source. This work treats the last and final section of the ESS linac, the Accelerator to Target (A2T), a transfer line, meaning no acceleration takes place, and therefore protons enter this section at their nominal energy of 2 GeV. The main diagnostics available at the end of the A2T are two Beam Position Monitor (BPM)s, the first of which is 3 m before the wall that separates the accelerator and target areas, and the second which is located exactly at the wall position. The separating wall imposes an aperture restriction, where the beam envelope must form a waist. The longitudinal position of the waist depends directly on the magnet settings in the A2T, and as such, if there are any errors in the beam line, the waist position will shift. The goal of this work is to investigate the viability of determining the beam waist longitudinal position using only the two final BPMs. Assuming a known set of Courant-Snyder parameters at the final position of the A2T and a known beam emittance, a set of final beam centroid positions are calculated lying over the 1sigma phase space ellipse at that point. Applying the initial condition that all beam centroids are initially placed at the origin, the necessary corrector strength values required to transport the centroids to their final positions along the ellipse are then calculated. Beam centroid trajectories are then compared with the beam envelope. Space charge effects are shown to be negligible for this session of the linac, meaning that the centroid envelope waist positions will coincide with the beam envelope waist positions. The two BPMs position readings are then used to calculate its longitudinal location. In this paper, a complete error study of the method is presented together with a discussion on its limitations.